Journal of
Manufacturing and Materials Processing

MDPI

Article

A Library of Mechanical Properties of Cu-CuAl Alloys Produced by Wire and Arc Additive Manufacturing

Filipa G. Cunha [1], Beatriz Nunes [1], Valdemar Duarte [1,2], Telmo G. Santos [1,3] and José Xavier [1,3,*]

[1] UNIDEMI, Department of Mechanical and Industrial Engineering, NOVA School of Science and Technology, Universidade NOVA de Lisboa, Campus da Caparica, 2829-516 Caparica, Portugal; fa.cunha@campus.fct.unl.pt (F.G.C.); bc.nunes@campus.fct.unl.pt (B.N.); valdemar.duarte@estsetubal.ips.pt (V.D.); telmo.santos@fct.unl.pt (T.G.S.)

[2] Polytechnic Institute of Setúbal, School of Technology of Setúbal, 2910-765 Setúbal, Portugal

[3] LASI, Intelligent Systems Associate Laboratory, Campus Azurém, 4800-058 Guimarães, Portugal

* Correspondence: jmc.xavier@fct.unl.pt

Abstract

This study aims to develop a library of Cu-CuAl material compositions and evaluate their mechanical properties. Various compositions are fabricated using Wire Arc Additive Manufacturing (WAAM) with GMAW and GTAW processes. The produced materials are characterised through hardness testing, eddy current measurements, and tensile testing supported by Digital Image Correlation (DIC). The hardness analysis reveals that increasing the CuAl content leads to higher hardness values. All compositions display stable and consistent eddy current measurements, except for the alloy with 25% Cu and 75% CuAl, which shows comparatively higher values. The load–displacement curves indicate that higher Cu content enhances ductility, resulting in a lower maximum load. Conversely, a higher CuAl fraction is directly associated with greater ultimate tensile strength. Overall, compositions with higher CuAl content exhibit improved mechanical performance, although they do not reach the levels of commercial materials due to defects inherent to the additive manufacturing process.

Keywords: Functionally Graded Materials; Additive Manufacturing; Mechanical Characterisation; Wire Arc Additive Manufacturing

1. Introduction

Copper (Cu) is a material with high electrical and thermal conductivity, good ductility and resistance to corrosion, which makes it an relevant material for electrical, thermal and structural applications [1,2]. However, Wire and Arc Additive Manufacturing (WAAM) with copper wire faces unique challenges stemming from its physical properties. Copper's high thermal conductivity promotes rapid and non-uniform heat dissipation during deposition, resulting in significant residual stresses, distortions and, in extreme cases, delamination of the deposited layers [3]. In addition, its high reflectivity makes stable heat transfer difficult, requiring greater energy input and increasing the chance of spattering, porosity and microcracks in the structure. The formation of oxides on the metal surface aggravates the situation, reducing the wettability and flow of the molten metal, which negatively impacts the integrity of the parts produced [4]. Defects such as porosity, humping, delamination and poor penetration into the substrate are common [4,5]. These problems underline the need to carefully tailor process parameters, such as welding voltage, current, pulse frequency, arc length and the use of Cold Metal Transfer (CMT) mode, to improve arc

Check for updates

Academic Editor: Guido Di Bella

Received: 11 December 2025
Revised: 14 January 2026
Accepted: 19 January 2026
Published: 22 January 2026

stability, reduce pores and ensure a more stable and dense deposition with copper wires [5]. Recent studies have shown that although it is possible to manufacture pure copper walls by WAAM, the components often have defects such as porosity, humping, delamination and oxygen segregation, compromising their final properties [4,6]. Strategies such as using CMT transfer modes, fine-tuning the current and pulse frequency, and implementing real-time monitoring systems have been explored to increase arc stability and reduce such defects [6,7].

In the case of copper alloys, the addition of aluminium (Cu-Al) has proved effective in increasing hardness and mechanical strength, albeit at the cost of a decrease in electrical conductivity due to the formation of intermetallic phases [5,8,9]. Recent work shows that progressively increasing the aluminium content leads to greater microstructural stability, greater tensile strength and greater hardness, confirming the potential of these alloys for structural and functional applications in extreme conditions [8,9]. In addition, the possibility of modulating composition gradients by WAAM makes the Cu-CuAl system particularly attractive for developing materials with graded properties, adjusted to specific performance requirements [10]. However, as with pure copper, the final microstructure of these alloys is strongly dependent on the welding parameters and interlayer thermal control, which directly affects their reproducibility and performance [5].

Recent reviews on copper-based alloys reinforce the relevance of these approaches, highlighting potential applications in highly demanding environments such as aerospace and maritime, and also emphasise the existing gaps. Among the main challenges are the need to reduce porosity, control microstructural heterogeneity, mitigate anisotropy and develop more effective post-processing protocols [2,11,12]. In addition, several studies point out that the lack of the standardisation of processing parameters makes it difficult to directly compare results between studies, which delays the transfer of technology to the industrial sector [2,11]. The integration of real-time monitoring strategies, such as computer vision systems or artificial intelligence algorithms, is beginning to show potential for anticipating and correcting defects during manufacture but is still far from being widely implemented [6,13]. From the point of view of mechanical characterisation, there is consensus that conventional methods do not adequately capture the local response in materials with composition gradients, which reinforces the growing importance of methodologies based on image correlation and inverse identification [5,8,14]. Thus, the literature converges in recognising that, despite advances in the manufacture of copper and Cu-Al alloys by WAAM, there is still no systematic database correlating composition, deposition parameters and resulting properties. In this context, the creation of property libraries covering hardness, mechanical strength and electrical conductivity as a function of Cu-CuAl composition represents an essential contribution to supporting modelling, process optimisation and the future integration of these alloys into high-performance industrial applications.

2. Materials and Methods

2.1. WAAM Apparatus and Procedures

The specimens analysed in this work were manufactured using the WAAM process. On the one hand, the printing of 100% Cu and 100% CuAl walls was successfully achieved using the Gas Metal Arc Welding (GMAW) process with a single wire as the primary feed material, as shown in Figure 1a. On the other hand, the Gas Tungsten Arc Welding (GTAW) process was employed with two wires to produce a homogeneous sample containing fractions of each Cu and CuAl constituent, as shown in Figure 1b. The experimental apparatus typically consisted of a welding power machine, a WAAM torch, shielding gas, a fume extractor and wire. The *G*-code programming language was used alongside the repetitive host software to control the printing movement in the x, y and z directions.

The utilisation of a welding power machine was a prerequisite for the execution of both processes. A Oerlikon CITOTIG 315 AC/DC welding machine was used for the GTAW and a Oerlikon CITOWAVE III 420 for the GMAW. Mild steel substrates were employed in this study, with dimensions of 250 mm × 50 mm × 8 mm (length × width × thickness). Two different feedstocks were used to fabricate the material compositions: DT-CuAg (copper) and ERCuAl-A2 (the Cu-Al alloy). The DT-CuAg feedstock had a diameter of 1.2 mm, while the ERCuAl-A2 feedstock had a diameter of 1 mm. The chemical composition of the wires is presented in Table 1.

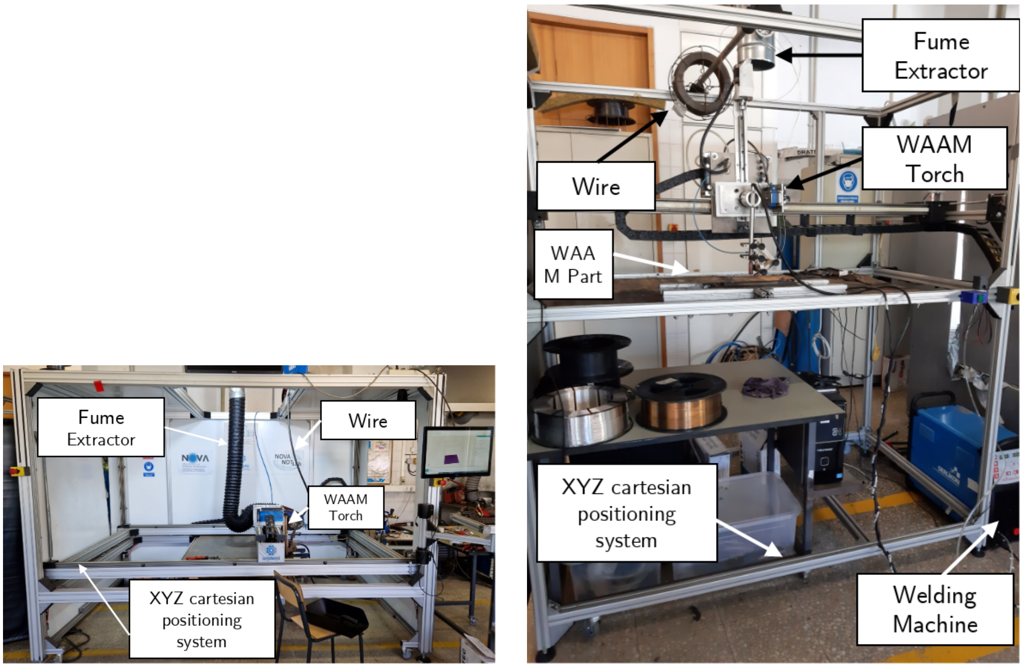

(a) (b)

Figure 1. Experimental setups for Wire and Arc Additive Manufacturing using (**a**) Gas Metal Arc Welding and (**b**) Gas Tungsten Arc Welding.

Table 1. Chemical composition of the wire feedstocks used in this work (wt.%) [15].

Material	Cu	Al	Fe	Ag	Mn	Ni
Cu (Dt-CuAg)	>99.0			1.0		
CuAl (DT-CuAl9Fe)	Rest	8.5	0.8		0.5	0.5

2.2. Deposition Strategy and Wall Construction

The length of the produced walls was set to 130 mm, and the contact-tip-to-work distance was 5 mm for the GTAW process and 10 mm for the GMAW process. According to the deposition strategy, after one layer had been deposited, the torch ascended by a distance equal to the height of a single bead and then automatically returned to the initial starting point. This process was repeated until a total height of approximately 50 mm was reached. Walls were produced for five different material compositions: 100% Cu, 75% Cu–25% CuAl, 50% Cu–50% CuAl, 25% Cu–75% CuAl, and 100% CuAl. For most compositions, three walls were fabricated, except for the 100% Cu and 100% CuAl cases, for which four samples were prepared as preliminary tests. Since each composition required distinct welding parameters, Table 2 summarises the travel speed, wire feed speed, interpass temperature, voltage, current, and number of layers used for each wall.

Table 2. Process parameters for different Cu-CuAl compositions with Wire and Arc Additive Manufacturing process.

Composition	Samples	Travel Speed [mm min^{-1}]	Wire Feed Speed [mm min^{-1}]	Interpass Temp. [°C]	Layers	Voltage [V]	Current [A]
100% Cu + 0% CuAl	4	450	500	80–100	27	19.6	156
75% Cu + 25% CuAl	3	95	712	250–350	19	18.3	160
50% Cu + 50% CuAl	3	100	875	250–350	20	17.8	150
25% Cu + 75% CuAl	3	100	875	250–350	20	18.7	150
0% Cu + 100% CuAl	4	300	400	100–150	27	17.6	77

The analysis of the deposition parameters revealed three distinct thermal regimes: the temperature range for pure Cu was 80–100 °C, for pure CuAl, it was 100–150 °C, and for Cu-CuAl mixtures, it was 250–350 °C. In the case of mixed compositions, elevated interlayer temperatures were required to ensure adequate cohesion. A direct correlation was observed between wire feed speed and travel speed: higher wire feed required lower travel speed, and vice versa, to stabilise the melt pool. It was also observed that at elevated interpass temperatures, increased wire feed and reduced travel speed facilitated enhanced local heat retention. Notably, higher CuAl fractions necessitated reduced travel speeds and tighter heat control to prevent defects. The mixed compositions were the most thermally critical due to their higher heat input and accumulated temperature, necessitating stricter process parameters to avoid overheating and distortion. The shielding gases used were pure Ar (99.999%) and a mixture of Ar + 1 % CO_2 + 18 % He at flow rates of 15 L min^{-1} to 18 L min^{-1} for samples produced by GMAW and GTAW, respectively.

2.3. Experimental Characterisation Techniques

After the production of all WAAM walls for the library, one end of each wall was sectioned to enable embedding in resin for subsequent hardness testing and eddy current measurements. The remaining portion of each WAAM wall was then machined using a Computer Numerical Control (CNC) system to produce specimens with a geometry specified according to DIN EN ISO 6892-1: Tensile testing of metals [16]. Figure 2a,b shows schematically the locations from which the specimens for each test were extracted.

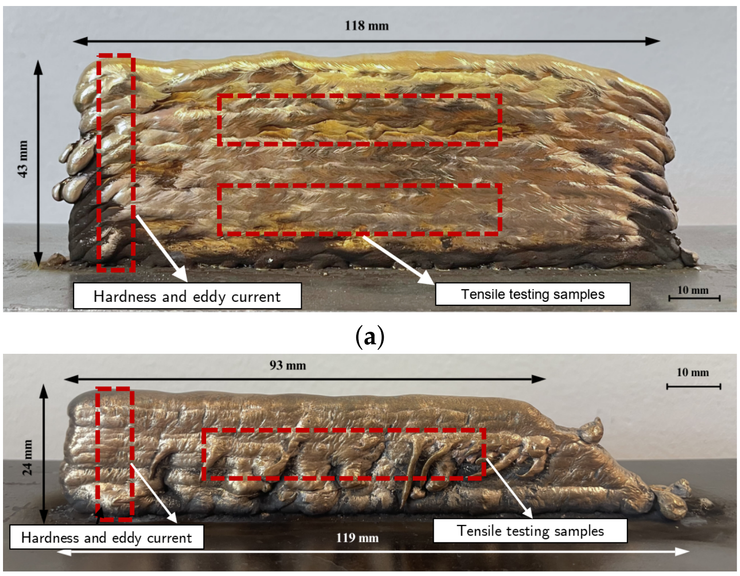

Figure 2. A schematic representation of the sample location for each characterization technique: (**a**) Gas Metal Arc Welding and (**b**) Gas Tungsten Arc Welding.

2.3.1. Microhardness Measurements

Microhardness indentations were made along the height of the sample, using the Mitutoyo HM-112 Micro-Vickers Hardness Testing Machine (Mitutoyo Corporation, Kawasaki, Japan). The load was 0.5 kg and the indentations were made over 10 s. The distance between indentations was 500 µm, starting from the substrate and continuing up to the final deposited layers.

2.3.2. Eddy Current Measurements

The eddy current measurements were performed on each of the samples. The experiment employed an absolute helical shielded EC probe, with a diameter of 3 mm, operating in bridge mode, and Olympus Nortec 500C impedance measurement equipment (Olympus Corporation, Tokyo, Japan). The measurements were obtained along a vertical line in the centre of the cross-section with a sample rate of 1 MHz. A customised probe positioning system with a precision of 0.1 mm was utilised. In all cases, the test frequency was set at 1.1 MHz, and the angle at 268° with the aim of aligning the variation in electrical conductivity with the imaginary axis. The gain was modified for each material to optimise the output signal.

2.3.3. Mechanical Property Measurements

Mechanical Tensile Tests

The STEP Lab 10 kN universal testing machine was used to carry out the tensile tests, as shown in Figure 3. The specimens were meticulously arranged in a vertical orientation and firmly secured within the grips of the apparatus. The tests were perfomed under displacement control, using a crosshead displacement rate of 1.5 mm min^{-1}.

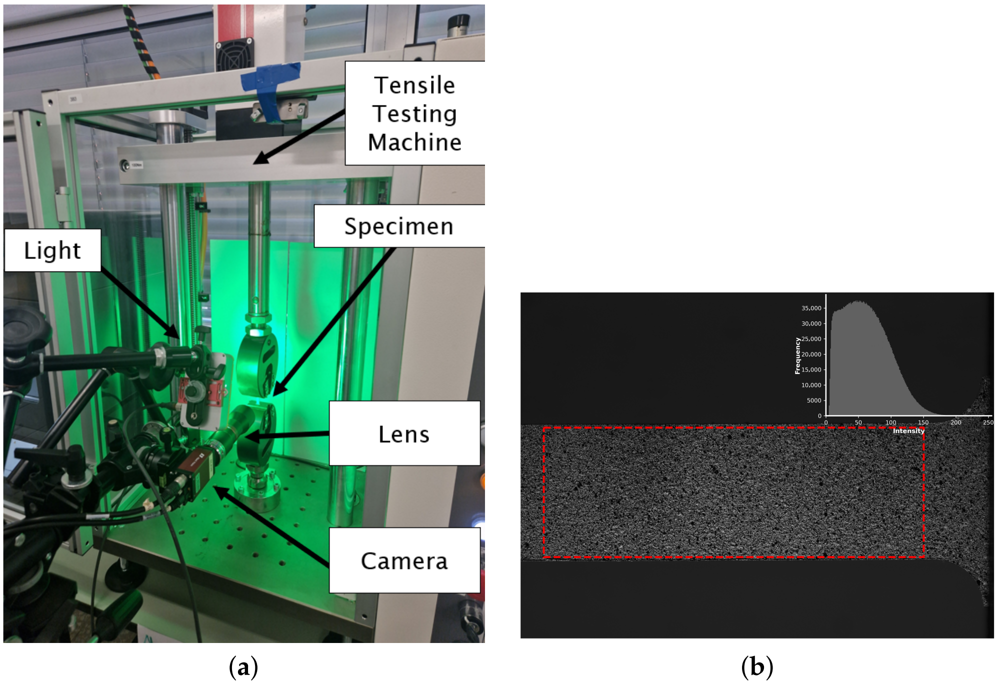

Figure 3. (**a**) Tensile test set-up with Digital Image Correlation; (**b**) applied speckle pattern with corresponding intensity histogram.

Digital Image Correlation Set-Up and Parameters

The tensile tests were coupled with the Digital Image Correlation (DIC) technique to capture full-field measurements across the central region of interest during the tests (Figure 3). A Manta G-1236 digital camera, coupled with a DTCM111-26-AL telecentric lens providing a field of view of 26 mm, was used. Table 3 summarises the components of the optical system employed. The required speckle pattern for the DIC technique was applied using an airbrush (Figure 3). A thin, uniform layer of matt white paint was first sprayed onto the surface, followed by the application of a random black speckle pattern using the airbrush.

Table 3. Optical system and 2D Digital Image Correlation setting parameters.

DIC Parameter	Specification
General DIC Settings	
Manta G-1236 Camera	4112 × 3008 pixels^2
Telecentric Lens	DTCM111-26-AL, 26 mm FOV
Conversion factor	0.00487 pixel/mmm
Average Speckle Size	8 pixels
Subset Size	51 pixels
Step Size	10 pixels
Shape Function	Affine
Interpolation Function	Bicubic Spline
Correlation Criterion	ZNSSD
Prefiltering	Gaussian (Kernel size = 5)
Strain	
Strain Window	5 data points
Virtual Strain Gauge (VSG)	91 pixels
Strain Interpolation Function	Bilinear Quadrilateral (Q4)
Strain Tensor	Green-Lagrange

The MatchID 2025.2.4 software [17] was used for image acquisition and DIC analysis. The Performance Analysis (PA) module of MatchID was employed to determine the most suitable DIC parameters for the analysis of the tested samples [18–22]. This study is summarised in Figure 4, where the ε_{xx} strain component at a selected point in the centre of the region of interest is plotted as a function of the Virtual Strain Guage (VSG). A convergence plateau was reached around VSG = 91 pixels. Table 3 summarises the DIC parameters defined according to the PA analysis and systematically applied to all tested specimens.

The strain measurements during the test were obtained as an average over a portion of the Region of Interest (ROI) [23]. Strain was measured across four distinct, concentric subregions corresponding to 100%, 75%, 50%, and 25% of the total ROI employed in the DIC analysis. The strain–time responses showed high consistency across the averaged subregions, confirming, as expected, the presence of uniform strain fields throughout the central portion of the specimens. Consequently, the full ROI was selected for all subsequent analyses.

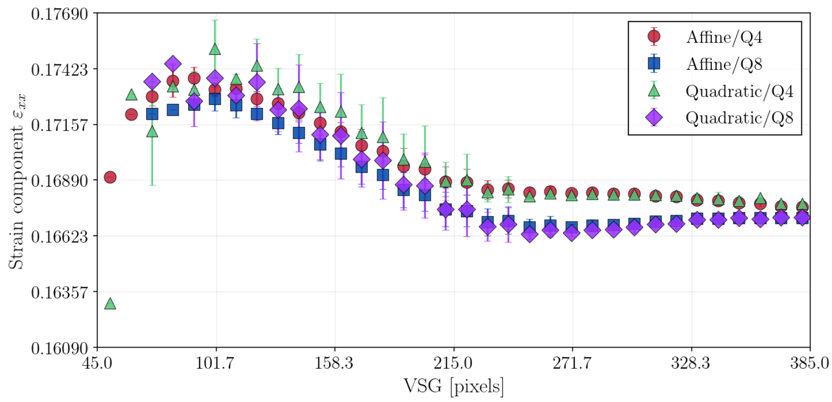

Figure 4. Performance analysis of the signal as a function of the virtual strain gauge in pixels.

Elastic Properties

The characterisation of the material's elastic behaviour was determined from the linear elastic part of the stress–strain curves. The elastic region was identified using an automated methodology that combines three analytical techniques: linear correlation analysis, derivative analysis, and the 0.2% offset method. The algorithm evaluates all three approaches and selects the one yielding the highest coefficient of determination (R^2), ensuring the suitable identification of the linear elastic behaviour.

An accordance with the ISO 6892-1 standard [24], for the Young modulus (E) calculation, a subset of the identified elastic region, between 10% and 50% of the elastic range, was used for linear regression. This methodological choice enhances accuracy by deliberately excluding the initial data points, which may be affected by measurement errors while the test machine's grips settle. Similarly, it avoids the upper limit of the elastic region, where the material may exhibit subtle non-linear behaviour just before yielding.

Both the Young modulus and the Poisson ratio (ν) were calculated using the linear regression of selected points within the elastic region. Young's modulus was determined from the slope of the stress–strain curve in the selected elastic range, while Poisson's ratio was calculated from the relationship between the transverse strain (ε_{yy}) and the longitudinal strain (ε_{xx}).

Constitutive Model Fitting and Plastic Properties

The engineering stress–strain curves, derived from the experimental load–displacement data coupled with DIC measurements, were analysed to characterise the material's plastic behaviour and determine appropriate constitutive model parameters. Therefore, the true stress (σ_t) and true strain (ε_t) values, which account for the instantaneous changes in the specimen's cross-sectional area during deformation, were obtained using the standard conversion equations [25]:

$$\sigma_t = \sigma(1+\varepsilon)\,, \quad \varepsilon_t = \ln(1+\varepsilon) \tag{1}$$

From the stress–strain curves, the 0.2% offset method was employed to determine the yield strength (σ_Y) and the ultimate strength from the ultimate loading.

To describe the plastic behaviour, stress–strains curves were fitted by two common strain-hardening models. The first model was the Hollomon power law [26], given by

$$\sigma_t = K\varepsilon_t^n \tag{2}$$

where σ_t is the true stress, ε_t is the true plastic strain, K is the strength coefficient, and n is the strain-hardening exponent.

The second model employed was the Ramberg–Osgood law [27], which relates the total strain to stress and provides a more comprehensive description across both elastic and plastic regions:

$$\varepsilon_t = \frac{\sigma_t}{E} + \left(\frac{\sigma_t}{H}\right)^{\frac{1}{m}} \tag{3}$$

where H is the Ramberg–Osgood strength coefficient, and m is the corresponding strain-hardening exponent. The fitting parameters for both models were determined through non-linear least-squares regression, with the quality of fit assessed using the coefficient of determination (R^2).

3. Results

3.1. Hardness Characterisation

The profiles of all material compositions, ranging from the substrate to the uppermost point of the cross-section, are shown in Figure 5. As it can be seen in the 100% Cu data (black points), this particular hardness profile is characterised by the lowest values, with an initial peak of 80 HV, subsequently decreasing to 40–50 HV across the majority of the cross-section. This 100% Cu profile displays a significant degree of variation in its vertical dimension, suggesting the presence of distinct zones characterised by varying microstructures. Such variations are likely attributable to the high levels of heat dissipation experienced, in addition to the potential presence of grain heterogeneity.

The 75% Cu–25% CuAl (dark blue points) demonstrates a relatively stable profile of 100 HV, with a decline to 70–80 HV. This initial constant hardness profile demonstrates microstructural uniformity following the initial deposition. It is evident that the material composition under scrutiny in this study exhibits a higher hardness profile in comparison with 100% Cu. This observation can be attributed to two primary factors: firstly, the reduced thermal conductivity and, secondly, the potential refinement of grains.

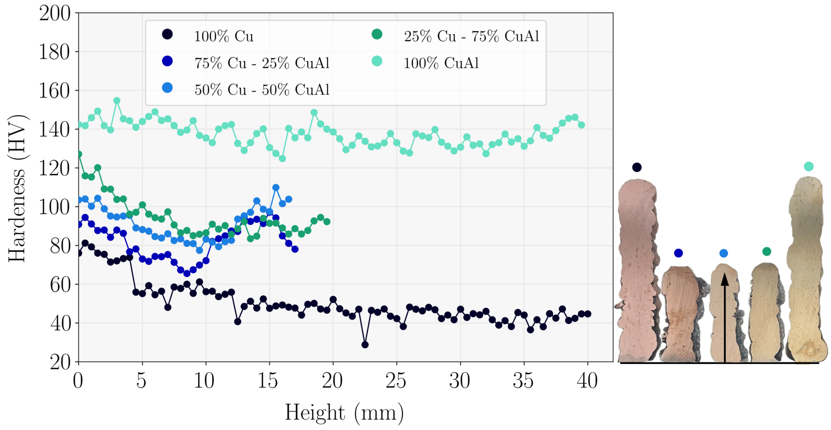

Figure 5. Hardness measurements taken from the substrate to the last deposited layer of the cross-section of all material compositions.

The hardness profile of the 50% Cu–50% CuAl composition material (cyan points) begins with hardness measurements of 100–110 HV, exhibiting a decline to 90 HV, accompanied by substantial fluctuations. These fluctuations are indicative of variations in heat or the presence of zones with heterogeneous microstructures, which may be attributable to the elevated interpass temperature of 250–350 °C.

The material composition 25% Cu–75% CuAl (dark green points) demonstrates a more stable profile, initially at around 120 HV, but then maintaining 80–110 HV throughout the cross-section. This smaller variation suggests that the welding process was more controlled and the microstructure more uniform.

The 100% CuAl (green line) is the material with the highest hardness (140–150 HV) and is very stable throughout the entire cross-section. This finding suggests that the material possesses a homogeneous and resilient microstructure, characterised by minimal heat dissipation and effective interlayer bonding.

In all Cu-rich compositions, a precipitous decline in hardness is evident after the initial few millimetres. This phenomenon may be attributed to the distinct solidification properties of the constituent layers. The initial layers, due to their rapid dissipation of heat to the substrate, undergo a swift solidification process, resulting in the formation of a finer (and consequently harder) microstructure. In contrast, the upper layers exhibit a slower rate of solidification, leading to the formation of thicker grains and a concomitant reduction in hardness. In CuAl-rich compositions, the hardness remains more uniform because the material retains more heat from the start, thereby reducing the thermal gradient between layers. In the context of CuAl-rich alloys, the maintenance of a homogeneous microstructure and constant properties is contingent upon the control of the heat of deposition and the reduction in thermal conductivity.

Figure 6 presents the correlation between the hardness (HV) of the samples and the relative percentage of copper (Cu). The experimental points, with their respective values, are connected by a solid black line, and a dotted line represents the linear fit of the experimental data. The linear fit equation is $HV = -0.747\%Cu + 128.728$, with a coefficient of determination, denoted by $R^2 = 0.895$. This indicates a strong correlation between the quantity of copper and the observed hardness. The average hardness values for copper concentrations of 0%, 25%, 50%, 75%, and 100% are 137, 95, 92, 82, and 50 HV, respectively.

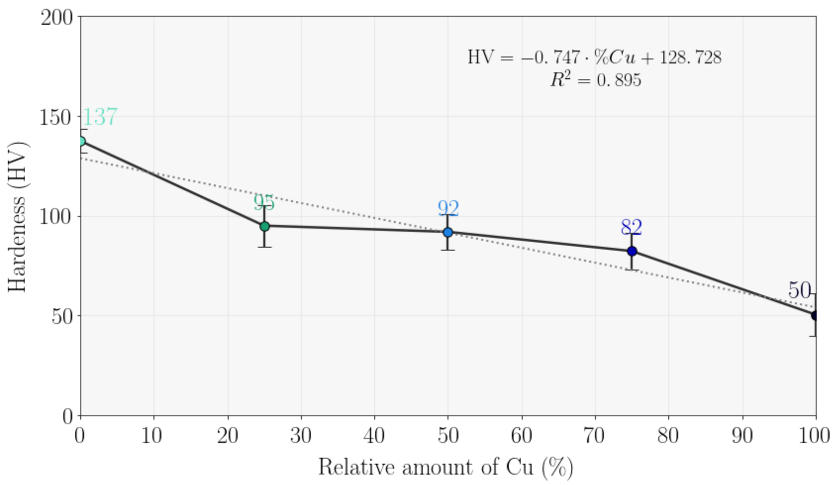

Figure 6. Mean hardness measurements of all material compositions.

3.2. Eddy Current Characterisation

Figure 7 shows the variation in eddy current response as a function of distance for each Cu–CuAl composition produced by WAAM. It is evident that the 100% Cu alloy exhibits relatively stable values, maintaining a constant level of approximately 2.0 throughout the entire measurement range. Intermediate compositions, such as 75% Cu–25% CuAl and 50% Cu–50% CuAl, exhibit slightly larger fluctuations, although these remain close to the same intensity level. Conversely, aluminium-rich alloys (25% Cu–75% CuAl and 100% CuAl) demonstrate a discernible trend, exhibiting considerably elevated eddy current values, with means exceeding 3.0. This discrepancy can be attributed to microstructural changes and electrical properties induced by compositional variations, which directly influence conductivity and, consequently, the response to eddy current testing. The figure displays a clear correlation between the aluminium fraction and the eddy current intensity; that is to say, the higher the copper–aluminium content, the higher the response. This behaviour provides relevant information for understanding the influence of composition on the electrical conductivity of alloys produced by WAAM, constituting important data for optimizing manufacturing parameters and developing applications where the electromagnetic response is crucial.

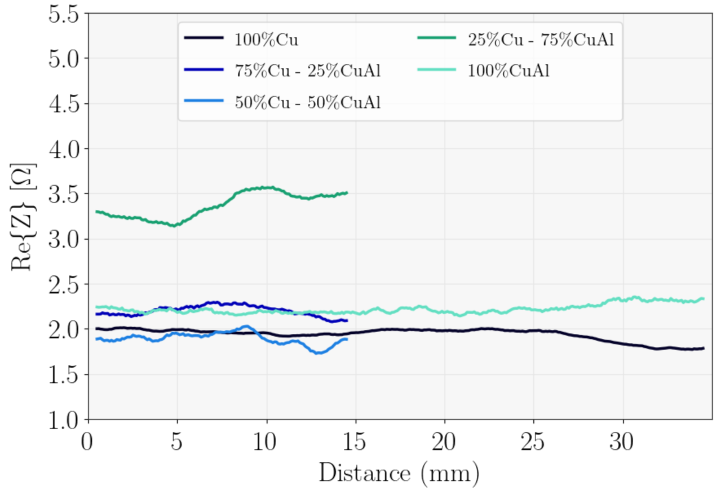

Figure 7. Eddy current measurements taken from the substrate to the last deposited layer of the cross-section of all material compositions.

3.3. Stress–Strain Behaviour from Tensile Tests with DIC

Figure 8 shows the load–displacement average curves for each material composition obtained from the tensile tests. As it can be seen, the 100% Cu material exhibits the lowest maximum load (1.8 kN) and moderate displacement (6 mm), while the 100% CuAl material demonstrates the highest maximum load (5.5 kN) and relatively high displacement (6.4 mm). The two mixed compositions display intermediate properties with a non-linear trend. The maximum load increases steadily with higher CuAl content, showing a clear positive relationship. In contrast, the maximum elongation does not follow a linear pattern across the different compositions.

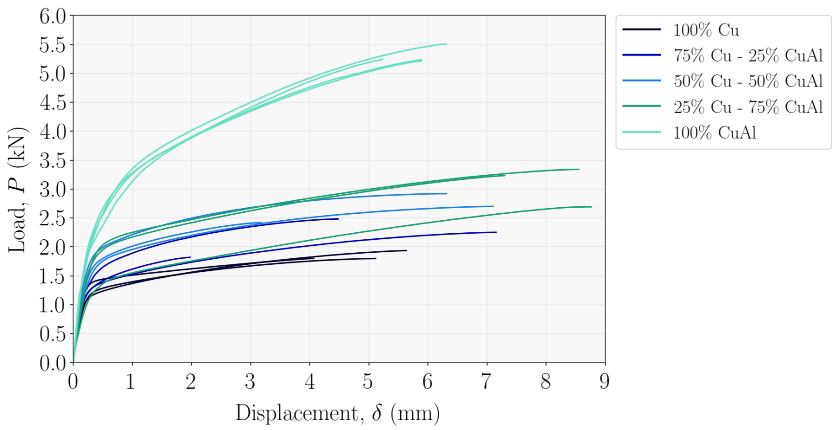

Figure 8. Load–displacement average curves for Cu-CuAl compositions under tensile testing.

As illustrated in Table 4, the maximum load, maximum displacement and average hardness for all material compositions are summarised. It can be concluded that the average hardness increases with increasing CuAl content.

Figure 9a shows the stress–strain average curves obtained for the different Cu-CuAl compositions produced by WAAM. A discernible trend of increasing mechanical strength is evident as the aluminium content is increased. The 100% Cu alloy demonstrates the lowest stress values, reaching approximately 250–300 MPa at the maximum strain considered. Conversely, aluminium-rich alloys, specifically those consisting entirely of CuAl, have been observed to attain levels in excess of 900 MPa, thereby demonstrating a notable enhancement in their mechanical properties. The intermediate compositions (75% Cu–25% CuAl, 50% Cu–50% CuAl, and 25% Cu–75% CuAl) demonstrate a progressive enhancement in their behaviour as the CuAl content is increased. This development underscores the strengthening effect of aluminium, in conjunction with microstructural modifications that result in enhanced hardening and increased load-bearing capacity. The findings demonstrate a favourable correlation between the CuAl content and the mechanical strength of the alloys, thereby substantiating the hypothesis that the material's ultimate properties can be modulated by manipulating its chemical composition. These data are relevant for understanding the potential of Cu-CuAl alloys manufactured by WAAM in applications requiring high mechanical strength, allowing for the optimization of composition selection according to specific structural requirements.

Table 4. Summary of maximum load, displacement at fracture, and average hardness for different Cu-CuAl compositions.

Composition	Max. Load (N)	Max. Displacement (mm)	Avg. Hardness (HV)
100% Cu	1799 ± 68	6.0 ± 0.7	52 ± 10
75% Cu + 25% CuAl	2251 ± 289	7.8 ± 1.4	79 ± 9
50% Cu + 50% CuAl	2419 ± 207	5.0 ± 0.6	83 ± 9
25% Cu + 75% CuAl	3232 ± 322	8.0 ± 0.1	99 ± 10
0% Cu + 100% CuAl	5507 ± 140	6.4 ± 0.5	138 ± 6

Figure 9b presents the transverse strain (ε_{yy}) as a function of the longitudinal strain (ε_{xx}) for all Cu-CuAl compositions. The slope of these curves represents the instantaneous Poisson ratio during deformation. All compositions exhibit an approximately linear relationship in the elastic regime, with the transverse strain becoming increasingly negative as the longitudinal strain increases, consistent with the expected lateral contraction under uniaxial tension. The 100% Cu composition displays the steepest initial slope, suggesting a higher Poisson ratio, whilst the CuAl-rich compositions exhibit somewhat shallower slopes. At higher strain levels, deviations from linearity become apparent, particularly for the intermediate compositions, which may be attributed to the onset of plastic deformation and localised strain heterogeneities. The 100% CuAl specimens reach transverse strains exceeding −0.14 at failure, corresponding to their higher longitudinal strain capacity. These full-field measurements obtained via DIC provide valuable insight into the multiaxial deformation behaviour of the Cu-CuAl alloys, complementing the uniaxial stress–strain characterisation.

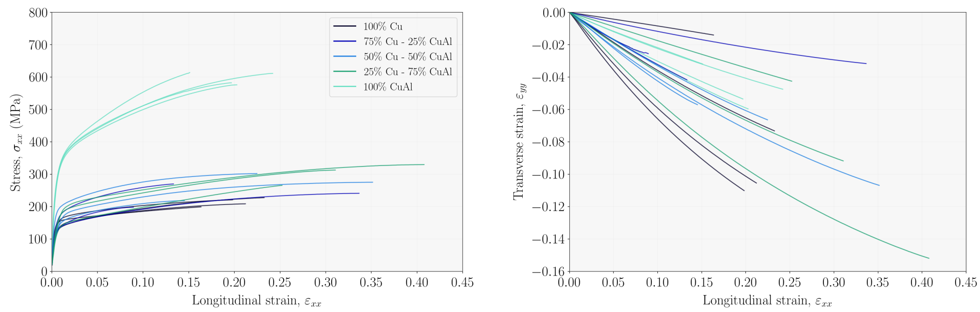

(**a**) (**b**)

Figure 9. (**a**) σ_{xx}–ε_{xx} and (**b**) ε_{yy}–ε_{xx} curves for Cu-CuAl compositions under tensile testing.

Figure 10a shows the yield strength (σ_Y) as a function of the specimen compositions. Pure copper specimens (100% Cu) yielded between 125 and 150 MPa, significantly exceeding the established literature value of 33.3 MPa for pure copper [28]. Conversely, the 100% CuAl composition exhibited a substantially higher yield strength, ranging from 259 to 286 MPa, a value approximately double that of the pure copper samples. This

https://doi.org/10.3390/jmmp10010042

finding is consistent with the literature data for pure CuAl, which reports a range of 269 to 293 MPa [29]. The intermediate compositions (75% Cu–25% CuAl, 50% Cu–50% CuAl, and 25% Cu–75% CuAl) displayed transitional behaviour, with their σ_y values distributed between those of the two pure materials. This systematic increase strongly suggests that the incorporation of aluminium into the copper matrix results in a pronounced solid solution strengthening effect.

Figure 10b plots the ultimate tensile strength, σ_u, as a function of Cu-CuAl material compositions. It can be concluded that σ_u increases progressively as the Cu content decreases, or conversely, as the CuAl content increases. The mean values are consistently below the reference lines for pure Cu (the dashed black line) and pure CuAl (the solid black line). This outcome is expected, as these materials are produced by WAAM and therefore exhibit microstructures and defects that differ from those found in commercial counterparts. The 100% Cu material exhibits the lowest σ_u value, within a range of 150–170 MPa, falling below the established reference value. The material composition, 75% Cu–25% CuAl, demonstrates a marginal increase in comparison to 100% Cu (180–210 MPa). The addition of CuAl has been demonstrated to enhance tensile strength. In the case of the intermediate material composition (50% Cu–50% CuAl), σ_u is approximately 200–240 MPa. This is in close proximity to the Cu reference line, indicating that the benefit derived from the CuAl addition compensates for the losses incurred due to overheating. For the composition material 25% Cu–75% CuAl, σ_u values are approximately 250–280 MPa. Finally, σ_u values for the 100% CuAl material is in the range of 450–480 MPa. However, these values were well below the reference value, likely attributable to the presence of internal defects characteristic of WAAM.

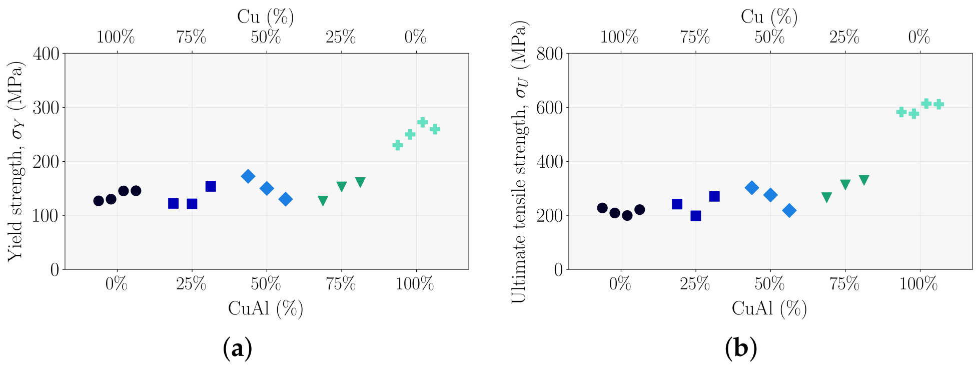

Figure 10. (**a**) Yield strength (σ_Y) of Cu-CuAl specimens with different material compositions. (**b**) Ultimate tensile strength, σ_u of Cu-CuAl specimens with different material compositions.

3.4. Elastic Behaviour: Young's Modulus and Poisson's Ratio

From the first data points in the linear elastic regime of the stress–strain curves, the Young's modulus and Poisson's ratio were calculated for each specimen. Figure 11a,b present the experimental results for these elastic constants across the different Cu-CuAl compositions, alongside reference values from the literature for pure Cu and pure CuAl. The acquisition rate of 1 Hz for image recording during tensile testing imposed limitations on the resolution of data points within the elastic region. This limitation, together with experimental uncertainties, led to considerable variability in the elastic constants obtained from the curve fitting.

Measurements of the Young Modulus (E) revealed a considerable scatter in values, ranging approximately from 20 GPa to 110 GPa, when compared to the reference values of 110–117 GPa for pure Copper and pure CuAl. Nevertheless, it was observed that the Young modulus progressively increases with aluminium content, suggesting an effect of partial solid solution strengthening and improved phase distribution. The 100% CuAl specimens displayed the highest moduli, approaching the theoretical value for wrought CuAl alloys, although all measured values remain below commercial references.

Regarding the Poisson Ratio (ν), the measurements also indicated significant scatter. Values ranged from approximately 0.08 to 0.67 compared to reference values of 0.34 for pure Cu and 0.33 for pure CuAl. Moreover, no clear trend was discernible in the Poisson ratio as a function of composition, with values fluctuating widely across all material compositions.

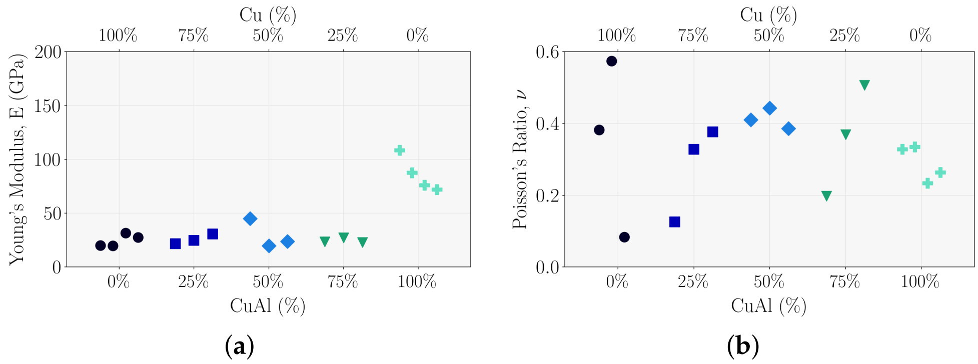

Figure 11. (**a**) Young's modulus of compositionally graded Cu-CuAl specimens; (**b**) Poisson's ratio of Cu-CuAl specimens across different compositions.

3.5. Plastic Behaviour and Constitutive Model Parameters

This section is concerned with the plastic behaviour of the Cu-CuAl library. The engineering stress–strain curves were first converted into true stress–strain curves so that the curve fitting of two established constitutive models, the Hollomon equation and the Ramberg–Osgood relation, could be performed.

Figure 12 presents the Hollomon law parameters for Cu-CuAl specimens with different compositions. The strength coefficient (K) increases markedly with higher concentrations of CuAl, ranging from 298–424 MPa for pure Cu to 1057–1217 MPa for pure CuAl, indicating that higher stress is required to cause plastic deformation in CuAl-rich alloys. The strain-hardening exponent (n) represents the material's capacity to harden upon deformation, with higher values suggesting a greater ability to distribute strain uniformly, thereby delaying the onset of necking. The results show some variability, but the values for all compositions are relatively low, characteristic of materials that do not exhibit extensive strain hardening. Pure CuAl specimens show slightly higher n values on average compared to pure Cu, suggesting a moderately enhanced strain-hardening capability.

Figure 13 presents the Ramberg–Osgood law parameters for Cu-CuAl specimens with different compositions, providing an alternative description of the stress–strain behaviour. The strength coefficient (H) increases significantly with the addition of CuAl, confirming the strengthening effect observed in the Hollomon model. Similarly, the strain-hardening exponent (m) shows a pattern analogous to n from the Hollomon law, reinforcing the characterisation of the material's hardening response. Both parameters exhibit trends consistent with the yield and ultimate tensile strength results, with H ranging from lower values for pure Cu to substantially higher values for CuAl-rich compositions.

The analysis of the plastic behaviour of the Cu-CuAl specimens reveals a consistent and predictable relationship between alloy composition and mechanical properties. The addition of aluminium to copper acts as a potent strengthening agent, leading to substantial increases in both yield strength and ultimate tensile strength. This is further corroborated by the strength coefficients (K and H) from both the Hollomon and Ramberg–Osgood constitutive models.

The strain-hardening exponents (n and m) are relatively low across all compositions, indicating limited strain-hardening capacity, although a slight increase is noted with higher

CuAl content. A degree of scatter is observable in the data, particularly for the intermediate compositions, which may be attributed to microstructural variations or inhomogeneities inherent in the manufacturing process of the alloy specimens. Overall, the results provide a comprehensive characterisation of the plastic response of these Cu-CuAl alloys, confirming the efficacy of solid solution strengthening and providing valuable parameters for engineering design and further material selection.

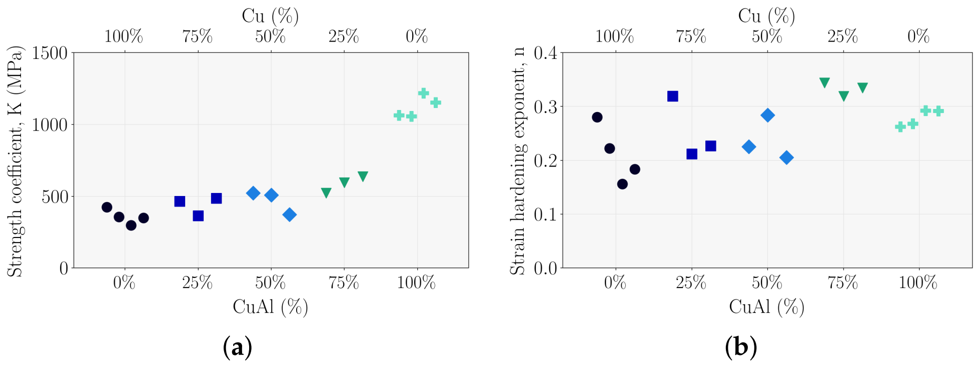

Figure 12. Hollomon law parameters for Cu-CuAl specimens with different compositions: (**a**) strength coefficient (K); (**b**) strain hardening exponent (n).

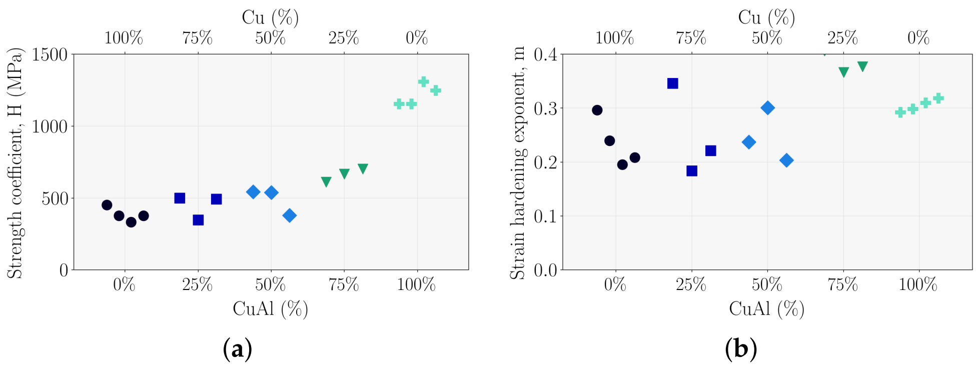

Figure 13. Ramberg–Osgood law parameters for Cu-CuAl specimens with different compositions: (**a**) strength coefficient (H); (**b**) strain hardening exponent (m).

4. Discussion

The findings of this study facilitate a more nuanced comprehension of the correlation between the Cu-CuAl composition and the mechanical performance of materials produced by WAAM. It was repeatedly demonstrated that increasing the CuAl proportion resulted in elevated levels of hardness and ultimate tensile strength [30,31], attaining values that surpassed those documented for pure copper. These results confirm the role of aluminium as a reinforcing element, promoting greater thermal and microstructural stability throughout the deposition process. However, it was found that the values obtained remained lower than those reported for equivalent commercial alloys. This is indicative of the influence of defects inherent to the additive manufacturing process, such as porosity, the lack of fusion, and solidification heterogeneity [32].

The hardness measurements revealed a strong linear correlation with composition (R^2 = 0.895), whereby hardness increased progressively from approximately 50 HV for pure copper to 137 HV for pure CuAl. This systematic trend reflects the strengthening effect of aluminium addition through solid solution hardening and the formation of intermetallic phases. The greater uniformity observed in CuAl-rich compositions suggests improved microstructural homogeneity, attributable to reduced thermal conductivity and more controlled heat dissipation during deposition.

The eddy current analysis revealed that copper-rich alloys exhibited stable values of approximately 2.0, whilst aluminium-rich alloys (containing a minimum of 75% CuAl) demonstrated significantly higher responses, with values exceeding 3.0. This marked increase in intensity with elevated aluminium content underscores the profound influence of composition on the electrical behaviour of WAAM-produced alloys, providing a non-destructive means of assessing compositional variations.

The stress–strain results clearly demonstrated that mechanical strength increases with aluminium content. Pure copper exhibited the lowest strength of around 250–300 MPa, whereas the 100% CuAl alloy surpassed 900 MPa. The strength of intermediate compositions increased progressively according to their CuAl fraction, confirming that the mechanical performance of WAAM-processed Cu-CuAl alloys can be effectively tuned through compositional control. Furthermore, the yield strength values for CuAl-rich compositions (259–286 MPa) were consistent with the literature data for wrought CuAl alloys, suggesting that the WAAM process can achieve comparable elastic–plastic transition behaviour.

Another salient aspect pertains to the impact of interpass temperature and deposition rate on the quality of the final component. Intermediate alloys (50–50% and 75–25%) were found to be of particular significance from a thermal perspective, as they necessitate more stringent parameters to avoid distortion and interlayer cohesion failures. This behaviour is directly reflected in the greater dispersion observed in the mechanical results for these compositions. Conversely, extreme compositions (100% Cu and 100% CuAl) exhibited more stable responses, albeit with distinct properties: copper maintained good ductility but low strength, whilst CuAl exhibited greater hardness and maximum load at the expense of greater deformation heterogeneity.

Notably, the most significant modifications to the deposition parameters were required for the pure compositions (Cu and Cu–Al). For intermediate compositions, only minor parameter adjustments were implemented, yielding comparatively small variations in thermal input. Hence, these limited thermal differences alone cannot account for the magnitude of the observed property variations, which correlate more directly with the systematic increase in Cu–Al content.

A comparison with the extant literature confirms these trends. Recent studies have indicated that, despite the potential of WAAM for producing alloys and materials with functional gradients, controlling microstructural heterogeneity remains one of the most significant challenges, particularly in the context of copper alloys due to their high thermal conductivity [8]. The results presented here serve to reinforce this conclusion whilst also demonstrating the relevance of advanced characterisation methodologies, such as DIC integrated with mechanical testing. Such methodologies permit the quantification of the local evolution of displacements and deformations with high spatial resolution, enabling a more rigorous assessment of material behaviour than conventional extensometry alone.

Finally, it should be noted that, although this work contributed a comprehensive library of properties for Cu-CuAl alloys produced by WAAM, some limitations remain. The considerable scatter observed in elastic property measurements (Young's modulus ranging from 20 to 110 GPa) is attributed to the limited temporal resolution of image acquisition within the elastic regime and the presence of process-induced defects. Furthermore, the absence of post-processing heat treatments and the lack of real-time monitoring techniques meant that it was not possible to reduce defects intrinsic to the process. In future work, the optimisation of deposition parameters, the integration of more robust thermal control strategies, and the combination with subsequent treatments may bring the results closer to the values of commercial alloys. Moreover, extending this methodology to other compositions and specific functional applications will contribute to consolidating the role of Cu-CuAl alloys as candidate materials for advanced structural and electrical applications.

https://doi.org/10.3390/jmmp10010042

5. Conclusions

The present study examined the fabrication of a library of Cu-CuAl material compositions utilising the WAAM technique. The samples were then analysed through hardness measurements and tensile tests with DIC. The following major conclusions can be drawn:

- A library of Cu-CuAl compositions produced by WAAM was created, ranging from pure copper to pure CuAl. This facilitated a systematic evaluation of the influence of the aluminium fraction on mechanical properties.
- It was observed that an increase in the aluminium content resulted in a progressive increase in hardness (from approximately 50 HV in Cu to approximately 150 HV in CuAl) and mechanical strength, although this was accompanied by greater microstructural heterogeneity.
- Eddy current measurements revealed stable responses ($\approx$2.0) for copper-rich compositions, whilst aluminium-rich alloys ($\geq$75% CuAl) exhibited significantly elevated values exceeding 3.0, demonstrating the influence of composition on electrical conductivity.
- Ultimate tensile strength increased consistently with CuAl content, from 150–170 MPa for pure Cu to 450–480 MPa for pure CuAl. Yield strength followed a similar trend, with values ranging from 125–150 MPa (pure Cu) to 259–286 MPa (pure CuAl).
- Copper-rich alloys exhibited greater ductility and homogeneous deformation, whilst aluminium-rich alloys demonstrated superior strength but increased susceptibility to plastic instability and localised fracture.
- The 25% Cu–75% CuAl composition exhibited an optimal compromise between strength (3.2 kN maximum load) and ductility (8.0 mm displacement at fracture), suggesting its potential for applications requiring balanced mechanical performance.
- Elastic property measurements presented significant limitations: Young's modulus values ranged from 20 to 110 GPa compared with reference values of 110–117 GPa, whilst Poisson's ratio varied widely from 0.08 to 0.67 (reference: 0.34 for Cu and 0.33 for CuAl). This substantial scatter was primarily attributable to the limited temporal resolution of image acquisition during the elastic regime (1 Hz recording rate), which prevented adequate data density in the linear elastic region, compounded by inherent noise in DIC measurements and process-induced defects in the specimens. Despite these limitations, a qualitative trend emerged suggesting Young's modulus increases with aluminium content; however, no clear compositional trend was discernible for Poisson's ratio. In contrast to these elastic property inconsistencies, the plastic behaviour characterisation (yield strength, ultimate tensile strength, and strain-hardening parameters) demonstrated robust and consistent trends across all compositions, confirming that the WAAM process reliably modulates mechanical strength through compositional control. Future validation of elastic properties via complementary techniques (with higher-frequency image acquisition) is recommended to establish reliable elastic constants for this material system.
- Constitutive model fitting demonstrated that the Hollomon strength coefficient (K) increased markedly from 298–424 MPa for pure Cu to 1057–1217 MPa for pure CuAl, confirming the strengthening effect of aluminium addition.
- Despite positive compositional trends, all mechanical properties remained below values reported for equivalent commercial alloys, indicative of defects inherent to the WAAM process, including porosity, lack of fusion, and thermal gradients.
- These findings underscore the viability of Cu-CuAl alloys produced by WAAM for structural and functional applications whilst highlighting the necessity to optimise deposition parameters and implement thermal or mechanical post-processing to mitigate defects and achieve performance comparable to industrial reference standards.

https://doi.org/10.3390/jmmp10010042

Author Contributions: Conceptualization—F.G.C., T.G.S. and J.X.; Methodology—F.G.C., T.G.S. and J.X.; Validation—F.G.C., B.N., V.D., T.G.S. and J.X.; Analysis—F.G.C., B.N., V.D. and J.X.; Investigation—F.G.C., B.N., T.G.S. and J.X.; Resources—T.G.S. and J.X.; Data Curation—F.G.C., B.N. and J.X.; Writing: Original Draft Preparation—F.G.C., B.N. and J.X.; Writing: Review and Editing—F.G.C., B.N., V.D., T.G.S. and J.X.; Visualization—F.G.C., B.N. and J.X.; Supervision—T.G.S. and J.X. All authors have read and agreed to the published version of the manuscript.

Funding: This research was funded by the Portuguese Foundation for Science and Technology (FCT, IP) under the following projects: TOP&AM4FGM—2022.06903.PTDC (https://doi.org/10.54499/2022.06903.PTDC, accessed on 10 December 2025); UID/00667: Unidade de Investigação e Desenvolvimento em Engenharia Mecânica e Industrial (UNIDEMI); and F.G. Cunha's PhD grant (https://doi.org/10.54499/2021.06889.BD, accessed on 10 December 2025).

Data Availability Statement: Data will be made available on request.

Acknowledgments: The authors have no additional acknowledgments beyond those listed in the Funding Section.

Conflicts of Interest: The authors declare that they have no known competing financial interests or personal relationships that could have appeared to influence the work reported in this paper.

Abbreviations

AM	Additive Manufacturing
BAMS	Bimetallic Additively Manufactured Structures
Cu	Copper
DED	Directed Energy Deposition
DIC	Digital Image Correlation
FGM	Functionally Graded Material
GMAW	Gas Metal Arc Welding
GTAW	Gas Tungsten Arc Welding
PA	Performance Analysis
ROI	Region of Interest
T-WAAM	Twin-Wire and Arc Additive Manufacturing
VSG	Virtual Strain Gauge
WAAM	Wire and Arc Additive Manufacturing

References

1. Deshmukh, P.S.; Tomar, K.; Sathiaraj, G.D.; Palani, I. Optimum strength and ductility of pure copper fabricated by Wire Arc Additive Manufacturing. *Manuf. Lett.* **2022**, *33*, 24–28. [CrossRef]
2. Morshed-Behbahani, K.; Aliyu, A.; Bishop, D.P.; Nasiri, A. Additive manufacturing of copper-based alloys for high-temperature aerospace applications: A review. *Mater. Today Commun.* **2024**, *38*, 108395. [CrossRef]
3. Baiocco, G.; Genna, S.; Salvi, D.; Ucciardello, N. Electrophoretic deposition of graphene coating on copper for improved thermoelectric performance of wire rods. *Int. J. Adv. Manuf. Technol.* **2024**, *133*, 5761–5776. [CrossRef]
4. Shah, A.; Gupta, N.K.; Aliyev, R.; Zeidler, H. Study of Various Process Parameters on Bead Penetration and Porosity in Wire Arc Additive Manufacturing (WAAM) of Copper Alloy Cu1897. *Appl. Sci.* **2024**, *14*, 9188. [CrossRef]
5. Fan, S.; Guo, X.; Li, Z.; Ma, J.; Li, F.; Jiang, Q. A Review of High-Strength Aluminum-Copper Alloys Fabricated by Wire Arc Additive Manufacturing: Microstructure, Properties, Defects, and Post-processing. *J. Mater. Eng. Perform.* **2023**, *32*, 8517–8540. [CrossRef]
6. Zhang, Q.k.; Yang, J.; Sun, W.s.; Song, Z.l. Evolution in microstructure and mechanical properties of Cu alloy during wire and arc additive manufacture. *J. Cent. South Univ.* **2023**, *30*, 400–411. [CrossRef]
7. Wang, P.; Nai, M.L.S.; Sin, W.J.; Lu, S.; Zhang, B.; Bai, J.; Song, J.; Wei, J. Effect of overlap distance on the microstructure and mechanical properties of in situ welded parts built by electron beam melting process. *J. Alloys Compd.* **2019**, *772*, 247–255. [CrossRef]
8. Dong, B.; Pan, Z.; Shen, C.; Ma, Y.; Li, H. Fabrication of Copper-Rich Cu-Al Alloy Using the Wire-Arc Additive Manufacturing Process. *Metall. Mater. Trans. B Process Metall. Mater. Process. Sci.* **2017**, *48*, 3143–3151. [CrossRef]

9. Kannan, A.R.; Rajkumar, V.; Vasudevan, S.V.; Jerome, P.; Oh, T.H. Microstructure, hardness, and electrical resistivity of Al-Cu alloy fabricated via wire arc additive manufacturing. *Mater. Today Commun.* **2024**, *39*, 108582. [CrossRef]
10. Rodrigues, T.; Bairrão, N.; Farias, F.; Shamsolhodaei, A.; Shen, J.; Zhou, N.; Maawad, E.; Schell, N.; Santos, T.; Oliveira, J. Steel-copper functionally graded material produced by twin-wire and arc additive manufacturing (T-WAAM). *Mater. Des.* **2022**, *213*, 110270. [CrossRef]
11. Vahedi Nemani, A.; Ghaffari, M.; Sabet Bokati, K.; Valizade, N.; Afshari, E.; Nasiri, A. Advancements in Additive Manufacturing for Copper-Based Alloys and Composites: A Comprehensive Review. *J. Manuf. Mater. Process.* **2024**, *8*, 54. [CrossRef]
12. Maleta, M.; Kulasa, J.; Kowalski, A.; Kwaśniewski, P.; Boczkal, S.; Nowak, M. Microstructure, Mechanical and Corrosion Properties of Copper-Nickel 90/10 Alloy Produced by CMT-WAAM Method. *Materials* **2024**, *17*, 50. [CrossRef] [PubMed]
13. Cunha, F.; Santos, T.; Xavier, J. In Situ Monitoring of Additive Manufacturing Using Digital Image Correlation: A Review. *Materials* **2021**, *14*, 1511. [CrossRef] [PubMed]
14. Henriques, J.; Xavier, J.; Andrade-Campos, A. Identification of Orthotropic Elastic Properties of Wood by a Synthetic Image Approach Based on Digital Image Correlation. *Materials* **2022**, *15*, 625. [CrossRef]
15. DRATEC Drahttechnik GmbH. Copper Wire Specifications. Available online: https://www.canman.ch/wp-content/uploads/2017/07/Copper_Wire_Specification.pdf (accessed on 7 April 2025).
16. *ISO 6892-1:2009*; Metallic Materials—Tensile Testing. ISO: Geneva, Switzerland, 2009.
17. MatchID, Version 2025.2.4. 2025. Available online: https://www.matchid.eu (accessed on 10 December 2025).
18. Lava, P.; Cooreman, S.; Coppieters, S.; De Strycker, M.; Debruyne, D. Assessment of measuring errors in DIC using deformation fields generated by plastic FEA. *Opt. Lasers Eng.* **2009**, *47*, 747–753. [CrossRef]
19. Cruz, D.J.; Xavier, J.; Amaral, R.L.; Santos, A.D. A Miniaturized Device Coupled with Digital Image Correlation for Mechanical Testing. *Micromachines* **2022**, *13*, 2027. [CrossRef] [PubMed]
20. Pereira, J.; Xavier, J.; Ghiassi, B.; Lousada, J.; Morais, J. On the identification of earlywood and latewood radial elastic modulus of Pinus pinaster by digital image correlation: A parametric analysis. *J. Strain Anal. Eng. Des.* **2018**, *53*, 566–574. [CrossRef]
21. Xavier, J.; Morais, J.; Pereira, F. Non-linear shear behaviour of bovine cortical bone by coupling the Arcan test with digital image correlation. *Opt. Lasers Eng.* **2018**, *110*, 462–470. [CrossRef]
22. Jones, E.M.C.; Iadicola, M.A. (Eds.) *A Good Practices Guide for Digital Image Correlation*, 2nd ed.; International Digital Image Correlation Society: Alexandria, VA, USA, 2025. [CrossRef]
23. Koerber, H.; Xavier, J.; Camanho, P. High strain rate characterisation of unidirectional carbon-epoxy IM7-8552 in transverse compression and in-plane shear using digital image correlation. *Mech. Mater.* **2010**, *42*, 1004–1019. [CrossRef]
24. *ISO 17296-2:2015*; Additive Manufacturing—General Principles—Part 2: Overview of Process Categories and Feedstock. ISO: Geneva, Switzerland, 2015.
25. Dowling, N.E. *Mechanical Behavior of Materials: Engineering Methods for Deformation, Fracture, and Fatigue*, 4th ed.; Pearson: Harlow, UK, 2013.
26. Hollomon, J.H. Tensile deformation. *Trans. Metall. Soc. AIME* **1945**, *162*, 268–290.
27. Ramberg, W.; Osgood, W.R. *Description of Stress-Strain Curves by Three Parameters*; Technical Report NACA Technical Note 902; National Advisory Committee for Aeronautics (NACA): Washington, DC, USA, 1943.
28. MatWeb LLC. Copper Cu Annealed. Available online: https://www.matweb.com/search/datasheet.aspx?matguid=9aebe83845c04c1db5126fada6f76f7e&n=1&ckck=1 (accessed on 7 April 2025).
29. MatWeb LLC. Copper UNS C61800. Available online: https://www.azom.com/article.aspx?ArticleID=6424 (accessed on 7 April 2025).
30. Ren, H.; Liu, Y.; Kong, H.; Song, C.; Xie, Y.; Sun, Q. Microstructure and mechanical properties of Al-Cu alloy during wire and arc additive manufacturing by adding micron TiB2 particles. *Virtual Phys. Prototyp.* **2024**, *19*, e2351170. [CrossRef]
31. Shah, A.; Zeidler, H.; Krinke, S. Investigation of process parameters in CuAl8 deposition under the influence of different material deposition angles via CMT-based WAAM process. In Proceedings of the Euspen's 23rd International Conference & Exhibition, Copenhagen, Denmark, 12–16 June, 2023.
32. Wang, J.; Shen, Q.; Kong, X.; Chen, X. Arc Additively Manufactured 5356 Aluminum Alloy with Cable-Type Welding Wire: Microstructure and Mechanical Properties. *J. Mater. Eng. Perform.* **2021**, *30*, 7472–7478. [CrossRef]